RSC Advances

ROYAL SOCIETY OF CHEMISTRY

www.rsc.org/advances

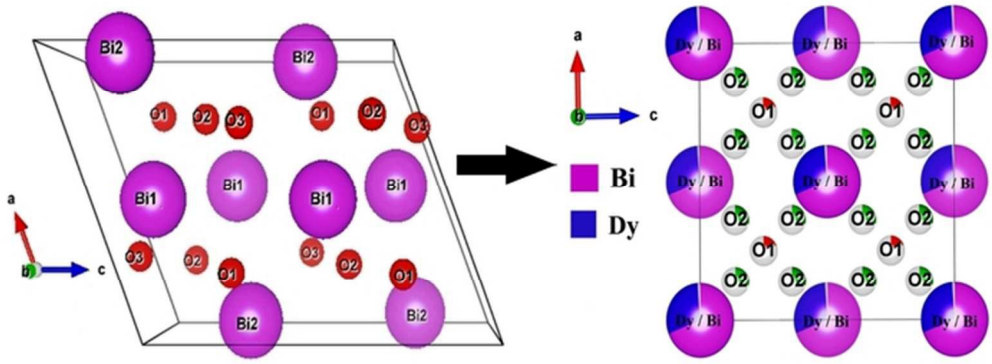

Structural conversion of Bi2O3 from monoclinic to FCC due to doping
29x11mm (600 x 600 DPI)

Microstructure and Charge Carrier Dynamics in Dy substituted phase stabilized cubic Bi_2O_3

Swagata Bandyopadhyay and Abhigyan Dutta*

Department of Physics, The University of Burdwan, Burdwan-713104, India

Abstract

Room temperature phase stabilization of cubic Bi_2O_3 has been achieved by adding Dy_2O_3 as dopant, using low temperature citrate-auto-ignition method. The samples were sintered at different temperatures retaining the cubic fluorite structure. Rietveld refinement of the X-ray diffraction profiles has given the detailed microstructural information of the prepared samples. The transmission electron micrographs confirmed the presence of atomic planes as obtained from X-ray diffraction. The Uv-Vis spectra show a red shift of the absorption peak with the increase in sintering temperature. Impedance spectroscopy studies of the samples exhibited thermally activated non-Debye type relaxation process. In addition, the studies of electrical conductivity have suggested the negative temperature coefficient of resistance (NTCR) behavior of the samples. The comparable values of activation energies, obtained from different parameters, indicated that the ions follow same type of mechanism for conduction as well as for relaxation. The temperature independence of the processes has been confirmed from scaling of different spectra. The correlation between structural and electrical properties of the samples has been discussed and interpreted accordingly.

Keywords: cubic-Bi_2O_3; Rietveld refinement; Transmission Electron Microscopy; Impedance Spectroscopy; Relaxation dynamics.

***Author for correspondence: Abhigyan Dutta**

Address: Department of Physics, The University of Burdwan, Golapbag, Burdwan-713104, INDIA email: adutta@phys.buruniv.ac.in **; Telephone: +913422657800; Fax: +91342 2634015**

1. Introduction:

In the family of solid oxide full cells (SOFC), Bi_2O_3 based materials have proven themselves as one of the most important members because of their superiority in oxide ion conductivity over conventional Ceria or Zirconia based ionic conductors [1-4]. Out of its different crystallographic polymorphs, interest has been centered on cubic δ-Bi_2O_3 because of its ability for highest oxygen ion conductivity among the family [5]. This cubic fluorite structure of bismuth oxide consists of a disordered oxygen sub-lattice with a short-range ordering of oxygen vacancies along the <111> direction [6]. The high ionic conductivity of δ-Bi_2O_3 is ascribed both to the large number of oxygen vacancies and high anionic mobility. The high concentration of oxygen vacancies (25% of the lattice sites) is a result of obtaining the cubic fluorite structure with Bi^{3+}cation. The high anionic mobility is related to the high polarizability of the Bi^{3+} cation with its lone pair of electrons [7]. However, this cubic phase is only stable in a narrow temperature range (730°C to melting point), and transforms to monoclinic α-phase through a dramatic phase transition [8]. The cubic phase at high temperature can be stabilized down to room temperature by the additions of dopants of comparable cation radii such as isovalent rare earth cations (Dy^{3+} , Ho^{3+}, Er^{3+}, Tm^{3+} , Yb^{3+}),Y^{3+}, WO_3 etc [1, 9]. However, these doped bismuth oxides show lower ionic conductivity and

undergo an order–disorder transition of the oxygen sub-lattice below 600°C, which leads to a time dependent decay in conductivity (aging effect) [6, 9].

A controversy on the stability of δ-Bi_2O_3 phase at room temperature aroused because Watanabe [10] claimed that, δ-Bi_2O_3 could not be stabilized by any oxide addition in long-term aspect. The stabilized bismuth oxides were treated as a quench-in phase or in other words, meta-stabilized phase. A systematic study [9] on the effects of different rare earth dopants on Bi_2O_3–Ln_2O_3 (Ln = Dy, Ho, Er, Tm and Yb) system showed that, the degradation rate of conductivity depends on the ionic radii and doping concentration. It was also observed that, two different mechanisms were responsible for degradation. One is phase transformation from fluorite to rhombohedral, which occurs most rapidly at about 650°C and the other one is the reversible order-disorder transformation of the vacancies, which occurs at about 500°C. It was shown that, the relative decay in conductivity is lowest for Dy_2O_3 stabilized cubic Bi_2O_3 [9, 11]. A recent study [12] on the energetic of doped Bi_2O_3 has also confirmed that, decrease in the volatility and susceptibility to reduction of bismuth oxide at high temperatures has been lowest for the Dy doping. Moreover, the dopant cations affect the nature of the vacancy arrangements in the oxygen sublattice and the polarizability of the cation affects the stability of the disordered oxygen sublattice [13, 14]. In a recent work [15] on Dy doped cubic bismuth oxide system; it has been shown that, the oxygen ionic conductivity has been much dependent on crystallite size, prepared through different synthesis routes.

In the present work, Bi_2O_3 is successfully stabilized down to room temperature and δ-phase has been found to be stable for long time duration. This has been achieved by singly doping of Dy_2O_3, keeping the as prepared sample at lowest possible sintering temperature for the lowest time duration.

The main objectives of this work are two folds. Firstly, to prepare the room temperature phase stabilized Dy doped cubic δ-Bi_2O_3 and secondly, to investigate the effect of sintering temperature on various structural, microsructural and ionic transport properties of prepared samples to enlighten new properties of this interesting solid electrolyte material. To the best of our knowledge, the analysis of electrical relaxation phenomena of this material has not been done yet.

2. Materials and methods:

Pure Bi_2O_3 and doped $Bi_{0.7}Dy_{0.3}O_{1.5-\delta}$ were prepared by low temperature citrate auto ignition method. For pure bismuth oxide, $Bi(NO_3)_3$, $5H_2O$ (MERCK, 99%) was used as precursor. First, the precursor was dissolved in 50 ml conc. HNO_3, diluted by 100 ml de-ionized water and the solution was stirred for 2 h at temperature 70°C. Citric acid (MERCK, 99.5%) in a 1:3 molar ratio with the Bi cations, was then dissolved in 200ml de-ionized water and added to the nitrate solution under constant stirring. It acts as a chelating agent as well as fuel for the reaction. The mixture was then stirred for 4 h at temperature 85°C. Due to constant evaporation, amount of sample became small (~50 ml) and the transparent solution became yellowish. After the homogeneous yellowish gel was formed, auto ignition process was completed within a minute and yellowish ash was produced.

For doped $Bi_{0.7}Dy_{0.3}O_{1.5-\delta}$, stoichiometric amounts of $Bi(NO_3)_3$, $5H_2O$ and Dy_2O_3 (ALFA AESAR, 99.9%) were used as precursors. First Dy_2O_3 was dissolved in 50 ml conc. HNO_3, diluted by 100 ml de-ionized water and the solution was stirred at 70°C temperature using magnetic stirrer for 1 h, until the solution became clear. After that, proper amount of weighted $Bi(NO_3)_3$, $5H_2O$ was mixed in the nitrate solution and again stirred for 2 h . Then citric acid at 1:3 molar ratios with the Bi cations was dissolved in 200 ml de-ionized water added to the

solution. The solution was stirred for 4 h at temperature 85°C. Due to constant evaporation the solution became yellowish and gel/foam was formed and auto-ignition process was completed within a minute and produced yellowish powder samples of doped compositions.

The agglomerated yellowish ash was crushed and grinded for 15 min for homogeneous mixing. The doped samples were divided into three parts and sintered at 600°C, 700°C, 800°C respectively and pure Bi_2O_3 was sintered at 600°C, each for 6 h duration with furnace cooling to room temperature. The samples are abbreviated as DSB1 (600°C), DSB2 (700°C) and DSB3 (800°C) respectively.

Powder X-Ray diffraction data were obtained at room temperature by X-ray diffractometer (BRUKER, Model D8 Advance-AXS) using CuK_α radiation (λ= 1.5414 Å) in 2θ range from 20°-80°, with step size 0.02° and scan rate 0.5 sec/step. The microstructure of the pure and doped samples were also studied using high-resolution transmission electron microscope (HR-TEM) (JEOL; Model: JEM-2010) operated at 200KV. For HR-TEM study, a pinch of powdered sample was dispersed ultrasonically in ethyl alcohol and a drop of colloidal solution was placed on a 300 mesh carbon coated Cu grid. The grid was dried over night under high power lamp.

Optical band gap of the pure and doped samples were determined from Ultraviolet-visible (Uv-Vis) absorption spectra, taken at room temperature using Shimadzu spectrophotometer (Model:1800), in the wavelength range 200-800 nm. For Uv-Vis study, powdered samples were dispersed ultrasonically in ethyl alcohol and ethyl alcohol was used as reference during the absorption measurement.

For electrical measurement, powdered samples were uniaxially pressed in a 10 mm diameter stainless steel die into cylindrical shaped pellets of average thickness about 0.17 cm.

Acetone was used as binder material. The pellets were annealed in air at 200°C for 2 h. The pellets were then polished to acquire smooth surface and high temperature conductive graphite pest (MERCK) was applied on both sides of the pellets to make the electrodes. Subsequently, the coated samples were annealed again at 200°C for 30 min.

Electrical measurements were performed by two probe method using an impedance analyzer (HIOKI; Model:3532-50) in the frequency range 42 Hz – 5 MHz and in temperature range 200°C - 440°C with 20°C step in air atmosphere inside a tube furnace.

3. Results and discussions:

3.1. X-Ray Diffraction and the Rietveld refinement:

Fig. 1(a) shows the XRD pattern of all the doped samples sintered at different temperatures. The well-indexed diffraction peaks indicate the single-phase cubic fluorite structure for all the samples. The XRD patterns were compared with standard data JCPDF card No.:71-2274 for pure sample and card No.:34-0376 for doped samples. XRD pattern of pure Bi_2O_3 confirms pure single monoclinic phase with space group $P_{2_1/c}$ and that of doped samples confirm the single-phase cubic fluorite structure with space group $F_{m\text{-}3m}$.

For Rietveld analysis, MAUD 2.33 [16] software has been employed. It is designed to refine simultaneously both the structural (unit cell parameters and atomic positions and occupancies) and micro structural parameters (crystallite size and r.m.s. strain). Various structural parameters including lattice parameter (a) and micro structural parameters like particle size (D), r.m.s. microstrain ($<\varepsilon^2>^{1/2}$) [17] have been refined by a standard least square method assuming the peak shapes as a pseudo-Voigt function [18, 19]. Instrumental broadening has been corrected by a specially processed standard Si sample. The background of the XRD patterns is

fitted with a polynomial of degree 5. The Marquardt least-squares method has been employed to minimize the difference between experimental and simulated patterns.

This minimization is monitored using two reliability index parameters R_{wp} (weighted residual error factor) and R_{exp} (expected error factor) defined as:

$$R_{wp} = \left[\frac{\sum_i w_i(I_0 - I_c)^2}{\sum_i w_i(I_0)^2}\right]^{1/2} \quad (1)$$

$$R_{exp} = \left[\frac{(N-P)}{\sum_i w_i(I_0)^2}\right]^{1/2} \quad (2)$$

Here, I_o and I_c are the experimentally observed and calculated intensities, w_i ($=1/I_o$) and N are the weight and number of experimental observations respectively and P is the number of fitting parameters. These values again lead to another closely monitored parameter namely goodness of fit (*GoF*) which is defined as: $GoF = \frac{R_{wp}}{R_{exp}}$. Refinement cycles are repeated until this *GoF* reaches a value near to unity. In the present case, *GoF* value remains within the range 1.30 to 1.68 which indicates good fitting quality for all these patterns.

The Rietveld refined patterns for pure Bi_2O_3 and Dy doped Bi_2O_3 samples are shown in Figs. 1(b) and (c) respectively. The monoclinic and cubic phase has been simulated by considering the COD file no. 9012546 and 9009850 respectively. Pure Bi_2O_3 contains single monoclinic phase with lattice parameter a = 5.8479 Å, b = 8.1660 Å, c = 7.5094 Å and $\alpha = \gamma = 90^0$, $\beta = 112.987^0$ and cell volume = 330.13(Å)^3. This monoclinic phase is converted into single FCC cubic fluorite phase with cell volume ~165(Å)^3. This decrease in cell volume with doping is due to the fact that ionic radius of Dy^{3+} (1.027Å) is lesser than the ionic radius of Bi^{3+} (1.17Å). The Rietveld analysis has exhibited that, no additional phase corresponding to Dy has been observed in the XRD profiles for the doped samples, which ensures the complete dissolution of the dopant into the host matrix. The sharp diffraction peaks in intensity as well as the narrow

spectral width indicate the high quality of crystallinity of the samples. The variation of crystallite size (D) and r.m.s. microstrain ($<\varepsilon^2>^{1/2}$) with sintering temperature of the doped DSB samples are shown in Fig. 1(d). From this figure, it is clear that, crystallite size (D) increases where as microstrain decreases with increase in sintering temperature.

The increase in lattice parameter and crystallite size with increase in sintering temperature indicates the grain growth of the samples with sintering temperature. This is because of the fact that, the thermal energy generates a force that reduces the total area of grain boundary. Due to the reduction of total area of grain boundary, the actual number of grains per unit volume decreases and grain size increases. This grain growth can further be explained by the following equation [20],

$$D^n - D_0^n = Kt \quad (3)$$

Where, D is the average grain size at time t, D_0 is the average initial grain size, n is the grain-growth exponent depending on the growth mechanism and K is a constant that could be expressed by the following relationship:

$$K = K_0 exp\left(-\frac{Q}{RT}\right) \quad (4)$$

Where, Q is the activation energy required for growth, K_0 is a constant, R is the gas constant and T is the absolute temperature.

Structural models of the pure and doped Bi_2O_3 samples have been generated using the atomic coordinates obtained from Reitveld analysis and the models are presented in Figs. 2(a) and (b) respectively. In the crystal structure of pure Bi_2O_3, as shown in Fig. 2(a), all the Bismuth atoms (Bi) are situated at the *4e* site with the atomic co-ordinate Bi1 (0.524, 0.1831, 0.3613), Bi2 (0.0409, 0.0425, 0.7762) and all oxygen atoms are situated at the *4e* sites with the atomic co-

ordinate O1 (0.78, 0.30, 0.71), O2 (0.242, 0.044, 0.134), O3 (0.271, 0.024, 0.513). All the atomic positions were fixed during the whole refinement process. When this pure Bi_2O_3 is doped with Dy atom, the monoclinic structure is converted into FCC cubic structure, which is shown in Fig. 2(b). Here all Bi and Dy atoms are situated at the *4a* site and oxygen atoms (O1 and O2) are situated at the *8c* and *32f* sites respectively. The Wyckoff position and fractional occupancy of the atoms for the sample DSB3 are listed in Table 1. Values of different structural and microstructural parameters like lattice parameter (a), cell volume (V), crystallite size (D), r.m.s microstrain ($<\varepsilon^2>^{1/2}$), R_{wp}, R_{exp}, GoF are listed in Table 2. The Rietveld refinement also shows that r.m.s. microstrain decreases with increase of sintering temperature which indicates the better stability of the samples with rise in sintering temperature.

3.2 Transmission electron microscopy analysis*:*

Further proof of crystallinity of the prepared samples has been given using room temperature high resolution transmission electron microscopy (HR-TEM) study. In Fig. 3(a), the nano-architecture of the sample DSB3 is shown with several hundred nanometers in the planar dimensions. All other samples also follow similar type of structural information. It can be inferred that, the process of sample preparation is sufficient to construct such type of flake nano-structures.

The orientation of the lattice plane is confirmed by using the simulated lattice pattern in Fig. 3 (b) with orientation along (200) direction. In the inset of Fig. 3 (b), the exact lattice spacing (d_{TEM}) ~ 0.296 nm is confirmed by the difference of the peak heights. This lattice spacing (d_{TEM}) value is comparable with that obtained from Rietveld analysis (d_{XRD}) for (200) plane of the same sample. The proof of crystal symmetry is given by using the selected area electron diffraction pattern as shown in Fig. 3 (c). In this figure, the bright and intense dots can be indexed in a cubic

cell and absence of intermediate small dots also confirms the phase purity even in the nano scale region. From this reciprocal lattice reconstruction of DSB3, it can be concluded that, the structure is not associated with any superstructure. The pattern in Fig. 3(c) has been found to be tilted at 2.6^{o} with positive x-axis. So the arrow heads are found to be tilted. Another high resolution TEM image of the sample is also shown in Fig. 3(d). To confirm the contributing lattice planes, we have also shown the fast Fourier transform (FFT) pattern in the left upper panel of Fig. 3(e) which is taken from the selected part of Fig. 3(d) as indicated by the red box. It can be confirmed from the distinct circular rings in the FFT image that, the contributing lattice planes are (200) and (220). The simulated lattice pattern signifies the different orientations of these two planes in the right upper and lower panel of Fig. 3(e). Further confirmation of cationic position is given by using the atomic model as shown in Fig. 3(f). Comparing with Figs. 3(d) and 3(f), it can be concluded that, Bi/Dy is localized at the same Wyckoff site and no distinction is possible due to their common site sharing.

3.3. Ultraviolet-Visible (Uv-Vis) spectroscopy*:*

The Uv-Vis absorption spectra for all the samples are shown in Fig. 4(a). The samples exhibited a distinct absorption band in UV-region (<400 nm). The optical band gap E_g can be determined by the classical tauc equation [21],

$$(\alpha . E_P) = A . (E_P - E_g)^q \quad (5)$$

Where, the symbols have their usual meaning. Fig. 4(b) shows the $(\alpha hv)^2$ vs hv plot of the sample DSB3 and band gap is determined by extrapolating the linear portion of this plot to $(\alpha hv)^2$ equal to zero. The obtained values of optical band gap (E_g) for prepared samples are listed in Table 3.

It may be found that, E_g decreases significantly with the sintering temperature from 2.46 *eV* to 2.07 *eV* for the doped samples in comparison with the pure one (2.71 *eV*).

In addition, the wavelength, at which the strong absorption occurs, decreases for the samples from Bi_2O_3 to DSB3. It exhibits the red shift of the spectra with the increasing sintering temperature. This red shift can be partially explained by the shrinkage of energy band gap with an increase in particle size [22]. The increased particle size due to grain growth at higher sintering temperature results in larger number of atoms in the particle causing the greater splitting of energy level resulting in the shrinkage of optical band gap. This is also consistent with the XRD results.

3.4 Electrical properties*:*

The ionic transport properties of the samples have been examined using impedance spectroscopy. The frequency dependent electrical properties of the materials can be expressed in terms of complex dielectric constant (ε^*), complex impedance (Z^*), complex electric modulus (M^*) and tangent loss ($tan\delta$). These quantities are related to each other by the following relations;

$$Z^*(\omega) = Z'(\omega) - j\,Z''(\omega) \tag{6}$$

$$\varepsilon^*(\omega) = \varepsilon'(\omega) - j\,\varepsilon''(\omega) \tag{7}$$

$$M^*(\omega) = M'(\omega) + j\,M''(\omega) \tag{8}$$

$$tan\delta = \frac{\varepsilon''}{\varepsilon'} = \frac{M''}{M'} = -\frac{Z''}{Z'} \tag{9}$$

Where, Z', M', ε' and Z'', M'', ε'' are the real and imaginary parts of impedance, modulus and permittivity respectively.

3.4.1 Impedance spectra analysis:

In general, the complex impedance spectra consist of two or three semicircular arcs as shown in the schematic representation in Fig. 5(a). The pictorial representation of the equivalent circuit required for explaining the various charge migrations and polarization phenomenon occurring in the sample is shown in the inset of Fig. 5(a). Here R_b, R_{gb}, R_e and Q_b, Q_{gb}, Q_e are the resistance and phase elements of bulk, grain boundary and electrode contribution respectively. 'Q' represents the modified capacitive phase element, deviated from the ideal behavior. The true value of capacitance (C) is calculated from the expression –

$$C = R^{\frac{1-a}{a}} Q^{\frac{1}{a}} \quad (10)$$

Where, a lies between 0 and 1. The fit using the equivalent circuit is done using EC-Lab software. In our experiment, most of the specimens exhibit a single semicircular arc (total impedance $R_{total} = R_b + R_{gb}$) at high frequency range with an extension (electrode contribution R_e) at low frequency range. Fig. 5(b) shows the complex impedance plot of DSB3 sample at different temperatures. The depressed and broad semicircular arcs indicate the presence of non-Debye type relaxation process. The same behavior has also been observed for all the other samples. The radius of the semi circular arc decreases with increase in temperature indicating increase in conductivity. This conductivity increment with the rising temperature may be due to the lowering of barrier for which mobility of charge carrier increases [23]. It also indicates that, the oxygen ion conduction in bulk and grain boundary region is a thermally activated process similar to that of semiconducting materials. This increase of conductivity with temperature is due to the increase of free oxygen vacancies i.e. most of the oxygen vacancies are free to migrate when measuring temperature increases. The variation of bulk conductivity (σ_b) and grain boundary

conductivity (σ_{gb}) with measuring temperature for the sample DSB3 is shown in the inset of Fig. 5(b).

Fig. 5(c) shows the complex impedance plots for all the samples at a fixed measuring temperature. This figure shows that, both bulk and gain boundary resistance decreases and total conductivity increases with increase of sintering temperature. The reciprocal temperature dependence of the total conductivity for all the samples are shown in Fig. 5(d) which obeys the Arrhenius equation given by,

$$\sigma = \frac{\sigma_0}{T} exp\left(-\frac{E_a}{k_B T}\right) \quad (11)$$

Where, σ_o is pre-exponential factor, E_a is the activation energy for electrical conduction, k_B is the Boltzman's constant and T is the absolute temperature. The values of activation energy ($E_{a\sigma}$), obtained from the slope of the curve in Fig. 5(d), are listed in Table 3.

It has been found that, the values of bulk and grain boundary resistance is much higher for the pure sample in comparison with the doped samples because, stabilization of the monoclinic Bi_2O_3 structure into cubic fluorite δ-Bi_2O_3 structure increases the number of oxygen vacancies to a great extent. In case of doped samples, total conductivity increases with increase in sintering temperature because, crystallite size increases which results in the decrease in grain boundary and consequently its contribution to the total conductivity. The increase of conductivity with sintering temperature can also be understood by measuring a term, called grain boundary blocking factor (α) which is expressed as, [24]

$$\alpha = \frac{R_{gb}}{R_t} \quad (12)$$

Where, R_{gb} is grain boundary resistance and R_t is total resistance. For each of the doped samples, α is calculated using the parameters obtained from the fitting of impedance spectra at a fixed measuring temperature and is found to decrease from 0.7937 to 0.6577 with rise in sintering temperature from 600^0C to 800^0C. Due to this decrease in blocking factor (α), grain boundary conductivity increases with increase of sintering temperature.

The different fitting parameters (a_i, R_i) obtained from complex impedance spectra and calculated values of capacitance (C_i) and conductivity for the bulk (σ_b) and grain boundary (σ_{gb}) contribution at 300^0C for the samples are listed in Table 4. For all the samples, the value of frequency exponent (a_i) for both bulk and grain contribution is less than unity ($a_i<1$), indicating the presence of non-Debye type relaxation for all the compositions.

Fig. 6(a) shows the frequency variation of the imaginary part of the complex impedance (Z'') at different temperatures for a particular sample (DSB3). Z'' value shows a peak maxima (Z''_{max}) at a particular frequency (relaxation frequency ω_{max}) and this peak shifts towards higher frequencies with increasing temperature indicating the presence of relaxation in the system [25]. The peak frequency ω_{max} is characterized by composition and structural arrangements of atoms in the sample.

Fig. 6(b) shows the scaling behavior of Z'' spectra. Here the frequency axis is scaled by relaxation frequency ω_{max} and Z'' is scaled by Z''_{max}. The spectra for all the compositions obey the time-temperature superposition principle (TTSP) i.e. all the Z'' spectra at different temperatures superimposed on a single master curve. This behavior simply indicates that, the change in temperature only changes the number of charge carriers without changing the conduction mechanism [26].

Using the value of ω_{max}, the relaxation time has been calculated using the equation,

$$\omega_{max}\tau = 1 \quad (14)$$

Where, $\tau = CR$, is the relaxation time.

Fig. 7 shows the variation of τ with reciprocal of absolute temperature. It has been observed that, the value of τ decreases with increase of measuring temperature for all the samples and its temperature dependence nature follows the Arrhenius relation given by,

$$\tau = \frac{\tau_0}{T} exp\left(-\frac{E_a}{k_B T}\right) \quad (15)$$

Where, τ_o is pre-exponential factor, E_a is the activation energy of electrical relaxation, k_B is the Boltzman's constant and T is the absolute temperature. The values of activation energy ($E_{a\tau}$) calculated from this plot are listed in Table 3 and shows a small but gradual decrease with increase in sintering temperature. These values are comparable with the previously reported values [14].

3.4.2. Modulus spectroscopy analysis:

Fig. 8(a) shows the frequency dependence of imaginary part of modulus $M''(\omega)$. An asymmetric maximum can be observed for $M''(\omega)$ at frequency ω_{max}. The asymmetric broadening of the peak indicates a spread of relaxation with different time constants, and hence the relaxation in the material is a non-Debye type. The region where the peak occurs is an indication of the transition from long-range to short-range mobility with increase in frequency.

The most probable relaxation time τ_m can be calculated from the peak frequency ω_{max} using the relation $\omega_{max}.\tau_m = 1$. The inset of Fig. 8(a) shows the reciprocal temperature dependence of ω_{max} for all the compositions which also obeys the Arrhenius relation.

The values of the activation energy for the most probable relaxation time (E_{τ_m}) obtained from the slope of the curves are given in Table 3 which again show the same type of variation

with the increase in sintering temperature. All the three types of activation energies ($E_{a\sigma}$, $E_{a\tau}$, E_{τ_m}) are found to be comparable with each other which indicates that the ions have to overcome the same barrier while conducting as well as when relaxing.

The scaling of the modulus isotherms is shown in Fig. 8(b) where the frequency axis is scaled by ω_{max} and $M''(\omega)$ is scaled by M''_{max}. The perfect overlap of all the curves on a single master curve at all temperatures indicates that the dynamical processes are temperature independent.

4. Conclusions:

Bismuth Oxide has been successfully stabilized into its cubic fluorite δ-phase at room temperature by doping of Dy_2O_3 using low temperature citrate auto-ignition method. X-ray diffraction analysis confirmed the cubic fluorite structure of the doped samples at room temperature. Various structural and microstructural parameters were estimated using Rietveld refinement of the X-ray diffraction profiles. It was found that crystallite size and microstrain exhibit opposite behaviour with increase in sintering temperature. The presence of different lattice planes and the proof of crystallinity was confirmed from HR-TEM study. The Uv-Vis spectra exhibited the red shift with sintering temperature because of grain growth of the samples. The complex impedance plots revealed that, both grain and grain boundary resistance decreased with rise in measuring temperature indicating the NTCR behaviour of the samples. The electrical relaxation processes occurring in the material have been found to be temperature independent. Comparable values of three types of activation energy indicate the single conduction mechanism. The conductivity, activation energy and other electrical properties were found to be strongly influenced by the sintering temperature of the materials.

5. Acknowledgements:

One of the authors (SB) thankfully acknowledges The University of Burdwan for granting state-funded fellowship. AD thankfully acknowledges the financial assistance from Department of Science and Technology (Govt. of India) (Grant no: SR/FTP/PS-141-2010). The authors (SB and AD) also acknowledge the instrumental support from DST (Govt. of India) under departmental FIST programme (Grant no: SR/FST/PS-II-001/2011) and University Grants Commission (UGC) for departmental CAS scheme.

6. Reference:

1 R. Punn, A.M. Feteira, D.C. Sinclair, C. Greaves, *J. Am. Chem. Soc.* , 2006, **128**, 15386-15387.

2 E.D. Wachsman, K.T. Lee, *Science*, 2011, **334,** 935-939.

3 D.W. Jung, K.L. Duncan, E.D. Wachsman, *Acta Mater*., 2010, **58**, 355–363.

4 K.T. Lee, H.S. Yoon, E.D. Wachsman, *J. Mater. Res*., 2012, **27**, 2063–2078.

5 M. Drache, P. Roussel, J.P. Wignacourt, *Chem. Rev*., 2007, **107**, 80-96.

6 E.D. Wachsman, S. Boyapati, M.J. Kaufman, N.X. Jiang, *J. Am. Ceram. Soc*., 2000, **83,** 1964-1968.

7 E.D. Wachsman, *J. Eur. Ceram. Soc*., 2004, **24**, 1281-1285.

8 M.J. Verkerk, K. Keizer, A.J. Burggraaf, *J. Appl. Electrochem*., 1980, **10**, 81-90.

9 N. Jiang, E.D. Wachsman, *J. Am. Ceram. Soc.,* 1999, **82**, 3057-3064.

10 A. Watanabe, *Solid State Ionics,* 1990*,* **40**, 889-892.

11 S. Boyapati, E.D. Wachsman, B.C. Chakoumakos, *Solid State Ionics,* 2001, **138**, 293-304.

12 T.B. Tran, A. Navrotsky, *Chem. Mater*., 2012, **24**, 4185-4191.

13 S. Boyapati, E.D. Wachsman, N. Jiang, *Solid State Ionics*, 2001, **140**, 149-160.

14 R. Li, Q. Zhen, M. Drache , A. Rubbens , C. Estournes , R.N. Vannier, *Solid State Ionics*, 2011, **198**, 6-15.

15 L.Lutterotti, MAUDWEB,Version2.33,http://www.ing.unitn.it/~maud/news.html.

16 B. Ghosh, S.K. Pradhan, *J. Alloys Compd*., 2009**, 477**, 127-132.

17 R.A. Young, in, *Introduction to the Rietveld method*, ed, R.A. Young, The Rietveld method, Oxford University Press; Oxford, 1993, pp. 1-38.

18 R.A. Young, D.B. Wiles, *J. Appl. Cryst*., 1982, **15**, 430-438.

19 S. Suwanboon, P. Amornpitoksuk, P. Bangrak, *Ceram. Int*., 2011, **37**, 333–340.

20 Sk. Anirban, A. Dutta, *J.Phys. Chem. Solids,* 2015, **76,** 178–183.

21 M. Elahi , D. Souri, *Ind. J. Pure & Appl. Phys*., 2006, **44**, 468-472.

22 T. Badapanda, V. Senthil, S.K. Rout, S. Panigrahi, T.P. Sinha, *Mater. Chem. Phys*., 2012, **133**, 863-870.

23 A. Rouahi, A. Kahouli, A. Sylvestre, E. Defay, B. Yangui, *J. Alloys Compd*.2012, **529**, 84-88.

24 R.M. Batista, E.N.S. Muccillo, *Ceram. Int*.2011, **37**, 1929–1934.

25 B. Behera, P. Nayak, R.N.P. Choudhary, *J. Alloys Compd*., 2007, **436,** 226-232.

26 S. Saha, T.P. Sinha, *Phys. Rev. B*., 2002, **65**, 134103.1-7.

Figure captions:

Figure 1: (a) XRD patterns of different doped samples with Bragg peak positions; Typical Rietveld refined output of the XRD patterns of **(b)** Pure Bi_2O_3 and **(c)** Dy doped cubic Bi_2O_3 samples [Experimental (I_o) data are shown as (o), simulated patterns (I_c) are shown by solid red lines, (I_o–I_c) (lower blue line) represents the corresponding difference for each of the pattern.]. **(d)** Variation of particle size and r.m.s. microstrain of doped cubic Bi_2O_3 samples with sintering temperature.

Figure 2: (a) Crystal structure of pure Bi_2O_3 sample possessing monoclinic structure. **(b)** Crystal structure of Dy doped stabilized δ-Bi_2O_3 sample possessing face centred cubic structure.

Figure 3:(a) A typical bright field TEM image of single nano-flack for the sample DSB3; **(b)** The simulated lattice plane with spacing 0.296 nm corresponds to (200) plane for the sample DSB3. In the inset the peak height and the difference between peaks corresponds to intensity of the lattice and the lattice spacing respectively; **(c)** The selected area electron diffraction pattern of DSB3 is shown along three perpendicular directions. The main diffraction dots of the cubic lattice lie at the intersections of the horizontal and vertical arrows directions. The zone axis is found to be tilted along 2.6^o **(d)** The lattice plane is shown for DSB3. The upper left in **(e)** corresponds to the fast Fourier transform (FFT) of the selected zone from (d) The circular rings in the FFT correspond to diffraction from two different lattice planes. The simulated planes are also found to be oriented along (200) and (220) directions. **(f)** The atomic model corresponds to the orientation of the cations in (d) with viewing direction along [100]. The blue and gray spheres correspond to Bi/Dy and O respectively.

Figure 4: (a) Uv-Vis absorption spectra of all the doped samples at room temperature. [Absorption spectrum of pure sample at room temperature is shown in inset] **(b)** Tauc plot for the sample DSB3; the calculated optical band gap for the sample is also shown.

Figure 5: (a) A model of impedance spectra for calculating different parameters. The equivalent circuit is also shown in the inset of the figure. **(b)** The complex impedance spectra for the sample DSB3 at different measuring temperatures. The variation of bulk (σ_b) and grain boundary conductivity (σ_{gb}) with measuring temperature is shown in the inset. **(c)** The complex impedance plot for all the compositions at a specific temperature. **(d)** Arrhenius plots of conductivity for all the samples.

Figure 6: (a) Frequency variation of imaginary part of impedance (Z'') at different temperatures for the sample DSB3 [The solid lines indicate the theoretical fit]. **(b)** Master plot or scaled curve of Z'' at different temperatures for the sample DSB3.

Figure 7: The variation of relaxation time with reciprocal of absolute temperature for all the doped Bi_2O_3 samples.

Figure 8: (a) The frequency dependence of M'' for the sample DSB3 at various temperatures [the solid lines indicate theoretical fit]. Inset shows the Arrhenius plot of the most probable relaxation frequency (ω_{max}) obtained from modulus formalism for all the samples [the solid lines denote the straight-line fit] **(b)** Master curve for M'' at various temperatures for the sample DSB3.

Table 1 : Refined Structural Data for the sample DSB3:

Atom	Wyckoff Position	Atomic coordinate (x,x,x)	Fractional Occupancy
Bi / Dy	*4a*	0	0.6932 / 0.2968891
O1	*8c*	0.25	0.18615
O2	*32f*	0.3617	0.29373

Table 2 : Composition wise values of lattice parameter (*a*), Cell Volume (*V*), crystallite size (*D*), r.m.s. micro strain ($<\varepsilon^2>^{1/2}$) and Rietveld refinement parameters R_{exp} (%), R_{wp} (%) and *GoF*. :

Sample Name	Lattice parameter *a* (Å)	Cell volume *V* (Å)^3	Crystallite Size *D* (nm)	r.m.s. microstrain $<\varepsilon^2>^{1/2}$ ($\times 10^{-4}$)	R_{wp} (%)	R_{exp} (%)	*GoF*
DSB1	5.4837	164.8988	40.53	17.10	16.5	12.64	1.30
DSB2	5.4852	165.0327	88.44	6.28	25.7	15.23	1.68
DSB3	5.4868	165.1833	121.40	2.73	20.4	15.25	1.33

Table 3: The values of total activation energy for dc conductivity ($E_{a\sigma}$), activation energy for relaxation ($E_{a\tau}$), activation energy for most probable relaxation time τ_m (E_{τ_m}) and optical band gap (E_g) for all the samples:

Sample Name	Activation energy for dc conductivity ($E_{a\sigma}$)(eV)	Activation energy for relaxation ($E_{a\tau}$) (eV)	Activation energy for most probable relaxation time τ_m (E_{τ_m})(eV)	Optical band gap(E_g) (eV)
Bi_2O_3	1.16	-	1.10	2.71
DSB1	1.17	1.16	1.17	2.46
DSB2	1.16	1.14	1.15	2.21
DSB3	1.15	1.11	1.13	2.07

Table 4: Values of frequency exponent (a_i), resistance (R_i), capacitance (C_i) and conductivity (σ_i) for the bulk and grain boundary contribution of all the samples at 300^0C:

Sample Name	Grain				Grain boundary			
	a_b	C_b(pF)	R_b(Ω) (x 10^4)	σ_b ($\Omega^{-1}.cm^{-1}$) (x 10^{-5})	a_{gb}	C_{gb}(nF)	R_{gb}(Ω) (x 10^4)	σ_{gb} ($\Omega^{-1}.cm^{-1}$) (x 10^{-6})
Bi_2O_3	0.98	35.36	20.49	0.11	0.97	0.15	24.64	0.87
DSB1	0.99	156.13	1.96	1.10	0.99	2.14	7.54	2.86
DSB2	0.98	158.95	1.86	1.16	0.82	31.50	6.29	3.43
DSB3	0.99	172	1.59	1.36	0.98	82.50	3.04	7.08

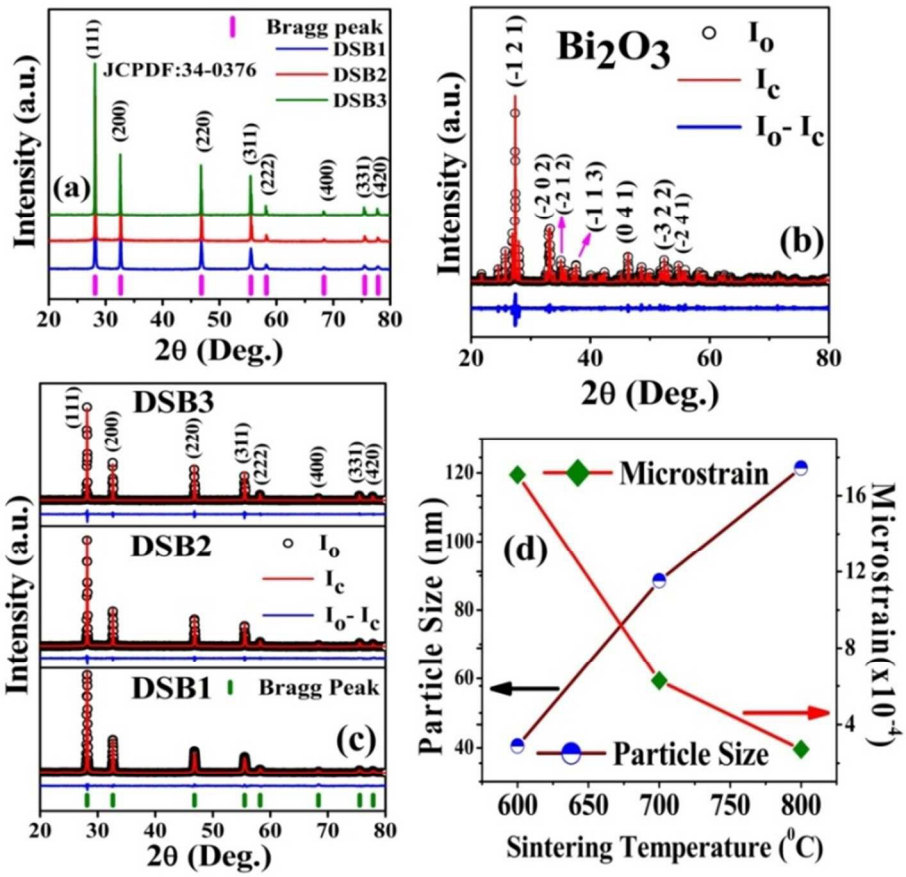

Figure: 1

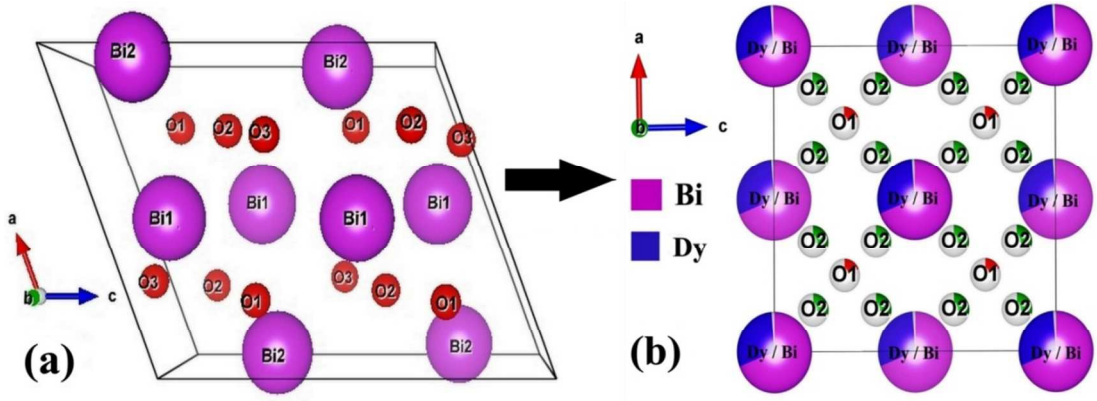

Figure: 2

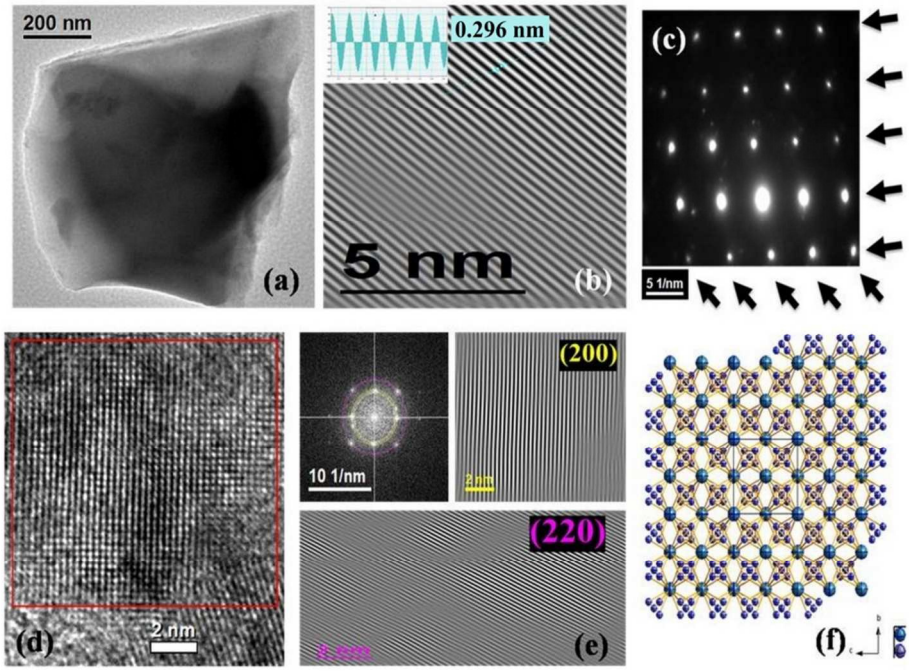

Figure: 3

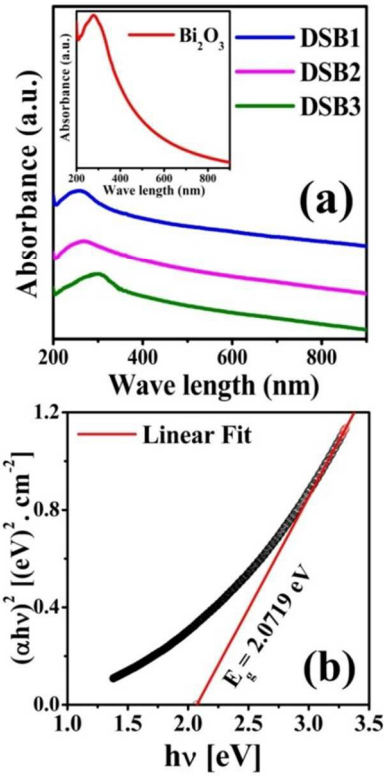

Figure: 4

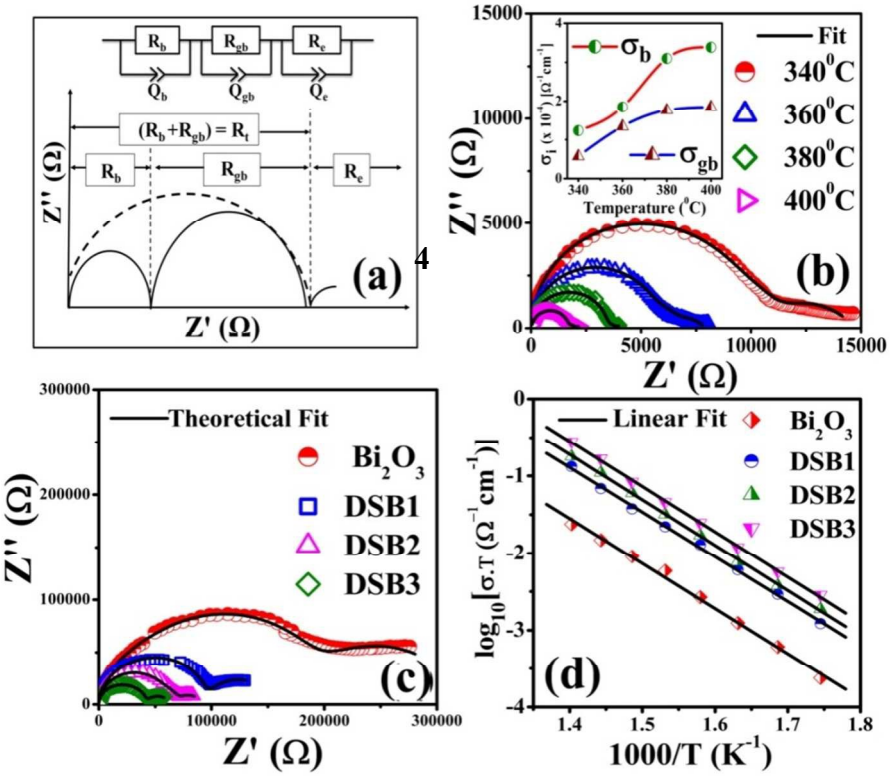

Figure: 5

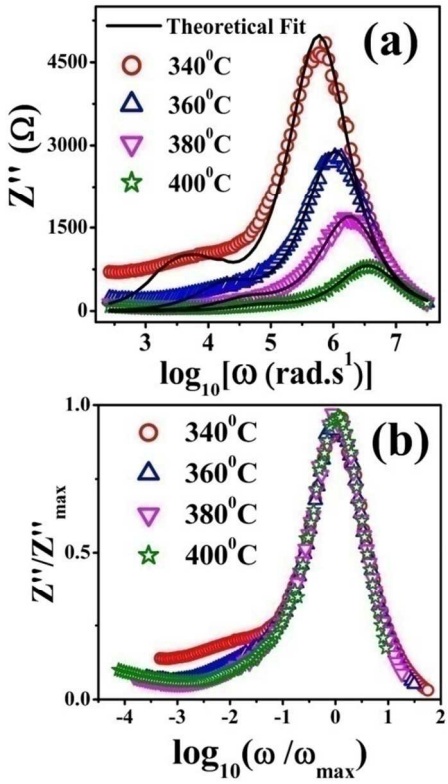

Figure: 6

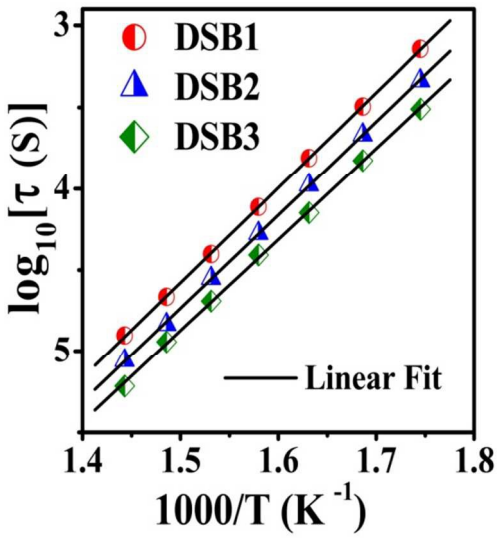

Figure: 7

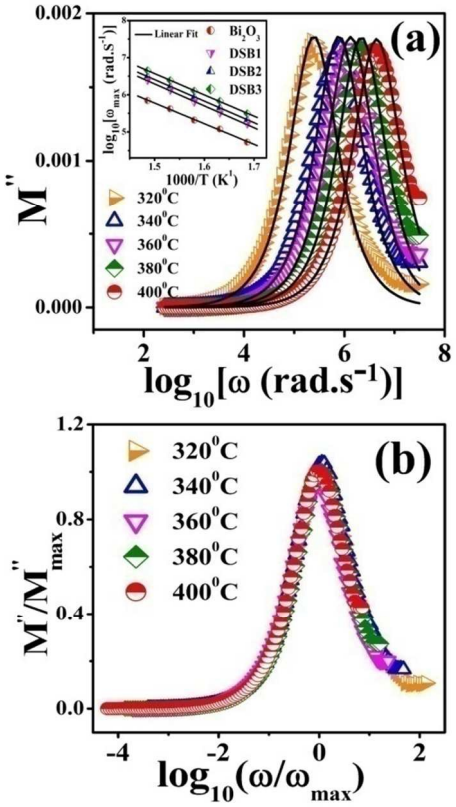

Figure: 8